

Super-Resolution Structured-Illumination X-Ray Microscopy based on Fourier Decomposition

Stefan Schwaiger^{1,2*}, Lennart Forster^{1,2}, Martin Dierolf^{1,2},
Franz Pfeiffer^{1,2,3}, Benedikt Günther^{1,2}

¹Chair of Biomedical Physics, Department of Physics, TUM School of
Natural Sciences, Technical University of Munich,
Paula-Hahn-Weinheimer-Str. 1, Garching, 85748, Bavaria, Germany.

²Munich Institute of Biomedical Engineering, Technical University of
Munich, Boltzmannstr. 11, Garching, 85748, Bavaria, Germany.

³TUM Institute for Advanced Study, Technical University of Munich,
Lichtenbergstr. 2, Garching, 85748, Bavaria, Germany.

*Corresponding author(s). E-mail(s): stefan.schwaiger@tum.de;

Abstract

We present a structured-illumination technique for full-field super-resolution transmission X-ray microscopy, which employs Fourier spectral decomposition inspired by established methods in visible-light microscopy. A 2D grating creating this illumination is stepped across one period to acquire a set of images at unique illumination positions. The Fourier domain of each image is described as a linear combination of replicated sample information at each frequency harmonic. As this superposition is created independently of detection, it contains spatial information exceeding native detector resolution. Recovering the encoded high-frequency components enables the population of an expanded frequency space. We demonstrate the presence of additional sample information in the Fourier spectrum and introduce a method to recover it. We achieve a resolution improvement by a factor of 2.2 for the projection image of a resolution test pattern. We further demonstrate seamless integration into standard X-ray tomography acquisition schemes. The acquisition is inherently multimodal, as phase-contrast and dark-field images can be computed from the same data using methods such as unified modulated pattern analysis, while providing an additional super-resolved transmission channel. These results indicate broad potential for non-destructive testing and biomedical imaging, as they alleviate pixel-size limitations in photon-counting detectors and sample-size restrictions imposed by optical magnification.

Keywords: imaging, tomography, X-ray, microscopy, super-resolution, structured-illumination, full-field, Talbot, synchrotron

1 Introduction

X-ray transmission microscopy is a widely researched technique due to its high spatial resolution and its ability to penetrate matter opaque to visible light. This is particularly relevant for non-destructive testing in fields such as additive manufacturing [1, 2] and battery engineering [3], as well as in biomedical research, including virtual histology [4, 5] and high-resolution imaging of small animals [6]. Achieving resolutions comparable to or exceeding those of visible light microscopy has been the focus of a large part of the body of research. Early efforts, such as those by Sievert et al. [7], proposed a methodology involving X-ray projection onto photographic film and subsequent magnification in a visible light microscope. First advances superseding this approach were made possible by better electron beam focusing optics, which enabled precise control of the electron spot size, thus reducing source blur. This was first realised by Cosslett et al. [8] in a transmission target configuration.

The refinement of X-ray transmission microscopy approaches towards their contemporary, well-established form was initiated by the development of X-ray optics, e.g., the KB-mirror [9], the compound refractive lens [10], and diffractive optics such as the Fresnel zone plate. Apart from typical geometric magnification microscopy, X-ray optics are generally applied in two distinct experimental geometries: full-field transmission X-ray microscopy (TXM) and scanning transmission X-ray microscopy (STXM). In a TXM setup, the sample is positioned at the focus of a condenser optic. The diverging beam is then refocused by an objective onto a 2D pixelated detector. In an STXM setup, the detector records the intensity transmitted through the sample at the focal point position. To image a larger section of the sample, it is scanned at multiple positions, with modern setups achieving resolutions of up to 30 nm [11]. Reaching such resolutions requires focal spot sizes in the order of 10 nm, which imposes stringent constraints on sample dimensions and acquisition time. Contrary to this limitation, Günther et al. [12] proposed a hybrid approach that merges STXM and Talbot array illumination. Rather than using an X-ray focusing optic to illuminate a single spot on the sample, the Talbot effect [13, 14] is employed to project an array of individual beamlets onto the sample. Scanning this array over a single period enables parallelization of the STXM scanning approach, thereby drastically reducing acquisition time. This method has been shown to achieve a resolution of several 100 nm [12].

In this publication, we propose structured-illumination super-resolution X-ray microscopy inspired by a well-established visible light microscopy technique [15, 16]. Contrary to Günther et al. [12], who treated the illumination as a collection of discrete focal spots, our method describes the illumination in terms of its Fourier spectral composition. The intensity distribution of a periodically structured illumination, generated with a grating by means of the Talbot effect [13, 14], is modulated by sample interaction and acquired on a 2D detector. The Fourier transform of the intensity

field at the detector plane prior to detection is described as a convolution of the sample's Fourier spectrum and a reciprocal Dirac comb, with frequencies determined by the pattern's fundamental frequency and its harmonics. Consequently, the intensity field is a superposition of replicas of the sample spectrum, with each replica shifted in Fourier space to the position of the peak that gives rise to it. Hence, around each peak in the reciprocal Dirac comb of the pattern, the same sample information populates the frequency landscape, except for a linear factor arising from the amplitude and phase of the peak. This frequency-space superposition is formed independently of detection, meaning it is present despite the optical transfer function (OTF) or the discretization introduced during detection. Therefore, accessing the additional information encoded in the superposition enables the reconstruction of a super-resolved image with an extended pass-band of $\mathbf{k}_n + N\mathbf{k}_p$, where \mathbf{k}_n is the native pass-band, N is the highest reconstructed order, and \mathbf{k}_p is the pattern frequency. To this end, a series of projections is acquired with varying positions of the illumination pattern. This defines a linear system of equations for which a synthesis matrix can be constructed, which assembles each projection from a basis described by the set of sample replicas. The solution of this set of equations produces a set of Fourier space images, each containing only the information contributed by a single replica.

After shifting the separated components to the origin in Fourier space and accounting for a linear factor, the components can be combined using a Wiener filter. This can be used to retrieve a sample image containing information surpassing the limits imposed by the OTF and the Nyquist frequency, provided the reconstruction sampling satisfies the Nyquist criterion for the super-resolved pass-band.

2 Results

2.1 Demonstrating the Presence of Additional Information

As a first step, we demonstrate the presence of additional information in an image of a resolution test pattern modulated by a structured illumination. Fig. 1 (a) displays an exemplary region in the modulated sample acquisition described in Sec. 3.3. The mean detected visibility over the full test pattern region is 23.9% following Eq. (22) and the procedure detailed in Sec. 3.3. (b) shows the modulation transfer function (MTF), with the 10% threshold marked by a white circle. (c) illustrates the logarithmic absolute value of the Fourier transform of the test pattern region. The zeroth-order component $C^{(0,0)}$ is centered around the origin of Fourier space. Thus, this component contributes information equivalent to an unmodulated native acquisition. The component $C^{(-1,0)}$ is centered around the peak of the Dirac comb positioned at the first-order harmonic of the grating in the respective dimension. The $C^{(-2,0)}$ component exhibits a more complex association. In the undetected intensity field, the center of the sample replica is at the corresponding integer multiple of the grating frequency. However, the detector samples this continuous signal with a finite number of discrete pixels. As this sampling is insufficient to resolve the second-order harmonic peaks, aliasing occurs, i.e., the peaks are wrapped to the opposite side of the pass-band.

Fig. 1 is in part organized as a grid: columns (d–f) correspond to components $C^{(0,0)}$, $C^{(-1,0)}$, and $C^{(-2,0)}$, respectively. Rows (i–iii) show (i) separated components, (ii) their

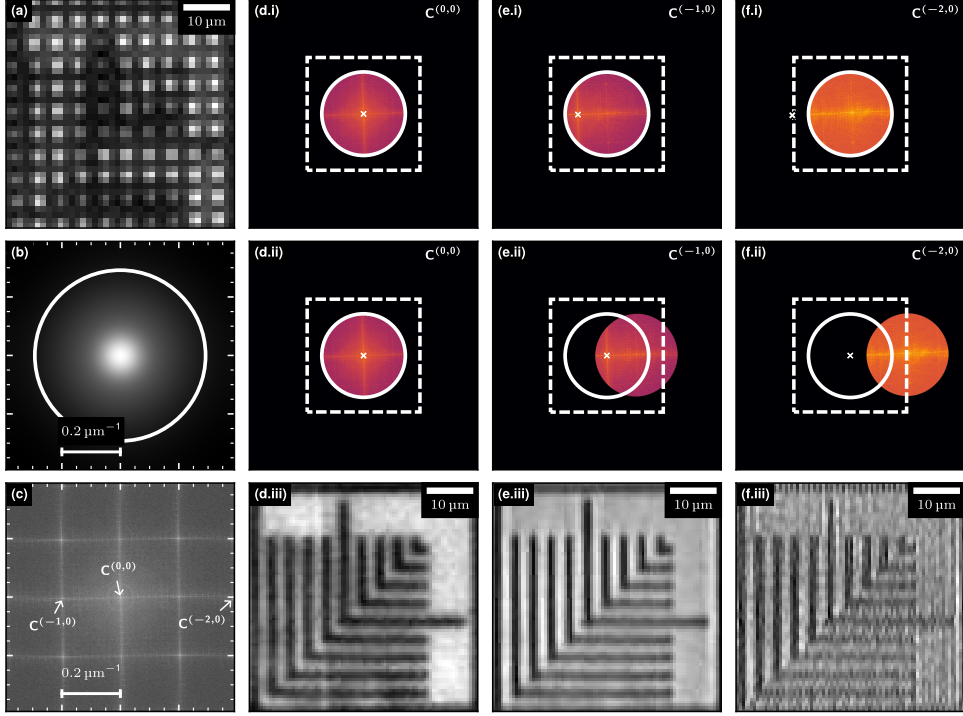


Fig. 1 Descriptive overview of the frequency landscape and its implications. (a) Exemplary region of the periodically modulated acquisition. (b) Modulation transfer function. The white circle indicates the region of support of $> 10\%$ modulation. (c) The logarithmic absolute value of the discrete Fourier transform of a single acquired image under structured illumination. Selected peaks in the Dirac comb are labeled. The second-order harmonic is marked at its aliased position. Each column (d–f) discusses an associated separated component marked in (c). The components are separated and zero-padded to twice their size to satisfy the Nyquist criterion for the super-resolved pass-band. The rows (i–iii) depict the same state for each component. (i) Separated components. Their information contribution is assumed to be zero outside of the region of support inferred from (b) and marked by the solid white circle. The additional constraint of the Nyquist frequency is shown by the white dashed square. The origin of each sample replica is marked by a white cross. (ii) The components of (i) shifted to their true position. The marked origin of the replica coincides with the origin of Fourier space. The shifted information exceeds both the previous region of support and the Nyquist limit. (iii) The absolute value of the inverse Fourier transform of (ii). Evidently, the feature modulation increases along the dimension of the shift vector.

true frequency positions, and (iii) a region-of-interest of their inverse Fourier transforms. The native resolution limits are marked in (i) and (ii) to illustrate how these components provide additional information. In visible light microscopy, the primary limitation to resolution is the diffraction limit $\frac{0.61\lambda}{\text{NA}}$ [14, 17], where λ is the imaging wavelength and NA is the numerical aperture. While this constraint also holds in X-ray imaging, other effects impose more stringent limits on resolution at wavelengths of the order of 1 \AA . One such effect is the OTF of the imaging system itself. It down-modulates high spatial frequencies, thereby curbing resolution. This region of support, defined as the region where the OTF permits intensities above the noise threshold, is

indicated by the solid white outline in rows (i–ii). Further, the maximum sampling frequency imposed by the detector pixel size restricts the resolution to the Nyquist limit, which is indicated by a dashed square in (i–ii). Overcoming this limitation is of great interest since imaging setups are typically well-optimized. Accordingly, a super-resolution method that merely compensates the OTF within the existing region of support offers limited benefit. Subfigure (d.i) displays the separated zeroth-order component, bounded by both the OTF and the Nyquist frequency. The absolute value of its inverse Fourier transform returns the unmodulated native detector image depicted in (d.iii). The aliased Fourier-space component in (f.i) is mapped to its unaliased position by an integer-pixel translation in the Fourier coordinate space, before being shifted to its true position shown in (f.ii). This is justified in Sec. 3.5.

Notably, high-frequency information, which lies outside the imposed resolution limit for the native image, is firmly within the region of support of higher-order components, allowing the population of an extended frequency space. The real-space implications are illustrated in row (iii), which presents the absolute value of the inverse Fourier-transformed components in (ii). The observed increase in pattern modulation along the direction of the component shift vector confirms the presence of additional high-frequency information.

2.2 Demonstration of Super-Resolution

The absolute value of the inverse Fourier transform of the separated zeroth order yields the unmodulated native detector image, which is used as a baseline to quantify the achieved resolution enhancement. In visible-light structured-illumination microscopy, the mean image over all pattern steps is typically used as the widefield equivalent [18]. However, to remove low-frequency modulation, this approach assumes that the pattern’s translation is perfectly equidistant. It is thus more appropriate to use the $C^{(0,0)}$ components, thereby alleviating the imposition of equidistance under the assumption that the separation matrix is well estimated. The precise steps taken in the reconstruction are detailed in Sec. 3.2.

As the reconstruction requires parameter estimation of an intensity field independent of detection, the effects of detection, specifically the point spread function (PSF), must be known precisely. It is reconstructed from an image of a circular aperture, as described by Forster et al. [19], and adequately modeled by the sum of two Gaussians with the mean widths of $\sigma_1 = 0.96 \mu\text{m}$ and $\sigma_2 = 3.32 \mu\text{m}$.

The super-resolution test pattern projection, reconstructed up to the second-order harmonic, is shown in Fig. 2 (a). The full test pattern projection for both the native and super-resolved cases is depicted in Extended Data Fig. 1 and 2, respectively. A comparison between first- and second-order reconstruction is depicted in Extended Data Fig. 3. The height map in Fig. 2 is normalized by a reference reconstruction. Subfigures (a–c) and (e–f) are all plotted on a common intensity scale. The line pattern marked by the light blue box is used for the modulation assessment in (d), the green square indicates the region-of-interest displayed in (b) and (c). Orange indicates the region used for the comparison in (e) and (f). An initial qualitative assessment can be made for the two enlarged regions of interest displayed in (b–c) and (e–f). When comparing the native scan in (b) to the super-resolved image in (c), the center of the

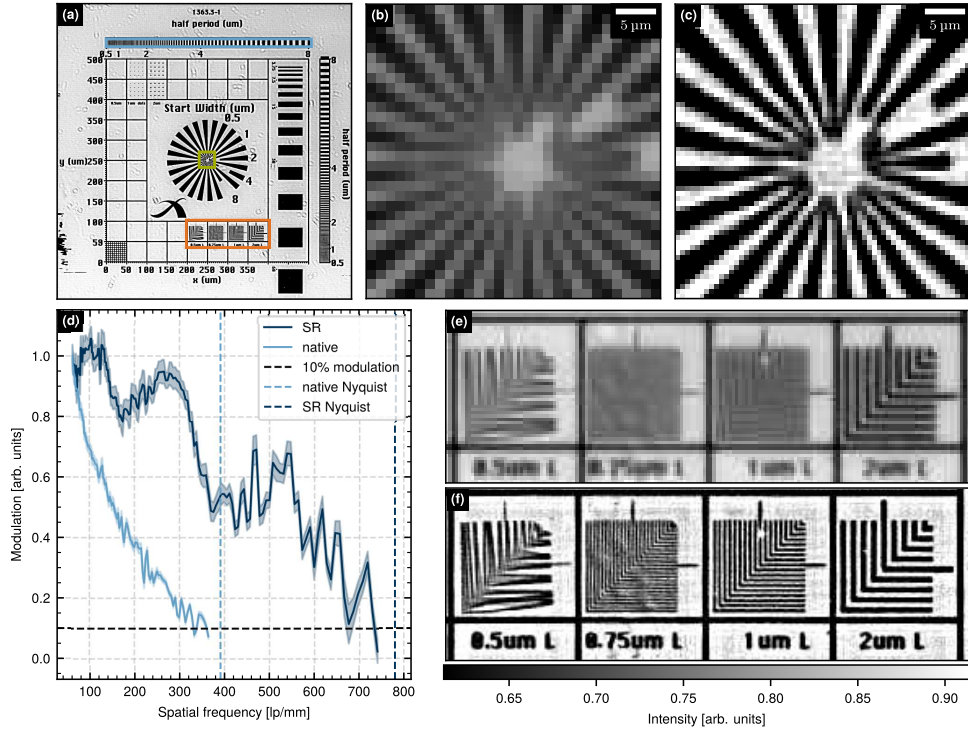


Fig. 2 Reconstruction and analysis for a resolution test pattern projection. (a) Reconstructed super-resolved projection of the pattern. The height map is normalized by a reference reconstruction. (b) Native image of the center region of the Siemens star in the middle of the test pattern marked in green in (a). (c) Second-order super-resolved image of the same region. (d) Modulation of the line pattern marked in light blue in (a) as a function of spatial frequency. The error margins indicate the propagated standard deviation of the noise. A modulation of 10% is chosen as the resolution criterion. The modulation in the reconstructed super-resolution (SR) images is superior across the entire frequency range and extends beyond the native Nyquist limit. (e) Native image of the L-shaped resolution target, marked in orange in (a). The 0.5 μm , 0.75 μm and 1 μm features are not resolved. The 2 μm features are well resolved. (f) Super-resolved image of the L-shaped resolution target marked in orange in (a). The 2 μm , 1 μm and 0.75 μm features are resolved. The 0.5 μm features remain unclear.

Siemens star shows a stark difference in modulation. Image (c) further demonstrates that the extended pass-band is populated isotropically, as the resolution gain shows no apparent directionality. The 2 μm line pattern in (e–f) is clearly resolved in both the native image and the reconstruction, with a native modulation at this resolution of 28.9% and a reconstructed modulation of 92.4%. The resolution gain is more readily apparent for the 1 μm pattern, as its feature size lies below the native effective pixel size of 1.28 μm . Accordingly, the native image does not resolve the pattern, while the reconstruction shows a modulation of 52.3%. This confirms the possibility of reconstructing information past the Nyquist limit of the imaging system. Similarly, the 0.75 μm line pattern is not resolved in the native scan, yet, although less so than the former, it is modulated in the reconstruction, which at this linewidth demonstrates a

modulation of 20.3 %. Contrary, the $0.5\ \mu\text{m}$ pattern is not resolved and further exhibits pronounced distortions. While this pattern irregularity may be exacerbated by Moiré artifacts, both the native and the reconstructed image show the same deformation morphology, so it is likely due to physical damage of the pattern. The quantitative modulation values in (d) are determined from the line pattern marked by the blue box in (a). For our purpose, a structure of a certain size is considered resolved if the modulation of the line pattern at this size exceeds 10 % [20]. Based on this criterion, the native resolution is 331 lp/mm, while the reconstructed resolution is 733 lp/mm. Hence, the resolution is increased by a factor of 2.2. The error margin is computed as the propagated error originating from the standard deviation of noise along the line pattern width. The effective pixel size in the reconstructed image is decreased to $0.64\ \mu\text{m}$ to satisfy the Nyquist criterion for the newly generated information components. As the line pattern frequency approaches the extended sampling frequency, the modulation values fluctuate depending on whether the modulation peak is distributed between two pixels or contained within a single pixel.

2.3 Super-Resolution Tomography

Beyond the resolution gain quantified on a projection image in Sec. 2.2, we demonstrate the applicability of our methodology for X-ray tomography. To this end, a tomographic dataset of a mouse skin was provided by John et al. [21]. The data acquisition and reconstruction are detailed in Sec. 3.4. Fig. 3 (a) shows an exemplary region of a native downsampled projection. Fig. 3 (b) shows the super-resolution reconstruction. Example regions from the tomographic reconstruction of both the native and super-resolved scans are depicted in (c) and (d), respectively. Under qualitative assessment of both the projection and the tomogram, the super-resolved reconstruction enables differentiation of features that are indistinguishable in the native scan. This is exemplified by the features highlighted by the red arrows in Fig. 3 (c) and (d). In the native tomographic reconstruction in (c), these features are indiscernible, while they are distinguishable in the super-resolved reconstruction in (d). This is quantified by the Fourier ring correlation [23] shown in subfigure (e). The correlation is computed between two neighboring projections, assuming that the angular difference is small enough to allow for correlation of the sample information. Up to the Nyquist frequency of $0.086\ \mu\text{m}^{-1}$ calculated from the native pixel size, the correlation of the super-resolved reconstruction follows the native correlation. The fundamental frequency of the structured illumination is $0.038\ \mu\text{m}^{-1}$, extending the recoverable information to $0.124\ \mu\text{m}^{-1}$, as confirmed by the correlation function. The second-order harmonic has a frequency of $0.077\ \mu\text{m}^{-1}$, which results in additional information up to $0.163\ \mu\text{m}^{-1}$. This is demonstrated again by the sustained correlation function over this interval. It supports the qualitative improvements seen in Fig. 3 (a–d), confirming that our super-resolution approach is effectively applicable for tomographic imaging.

2.4 Discussion

In this proof-of-principle, we demonstrated a full-field super-resolution reconstruction approach for a test pattern projection up to the second-harmonic order of a square

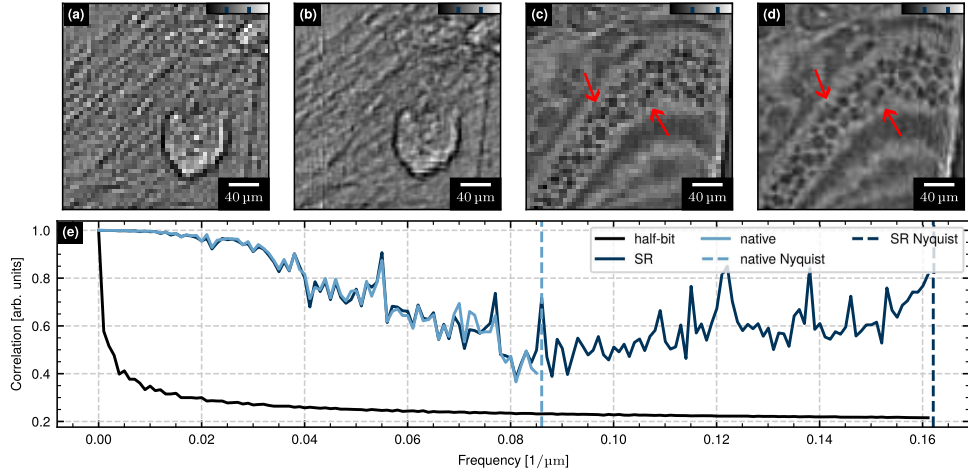


Fig. 3 Native and super-resolved tomographic reconstruction. (a) Native downsampled projection. (b) Second-order super-resolution reconstruction of the downsampled projection. The colorbars in (a) and (b) are marked at 0.7 and 1.1 in arbitrary units of normalized intensity. (c) Region-of-interest in a tomographic slice of the native downsampled reconstruction. (d) Region-of-interest in a tomographic slice of the second-order super-resolution reconstruction of the downsampled projections. The red arrows in the tomographic reconstructions highlight features that are indistinguishable in the native image in (c) but become discernible in the super-resolved image in (d). The two ticks in the colorbars in (c) and (d) mark the linear attenuation at 0 and 10 in units of mm^{-1} . (e) Fourier ring correlation computed on (a) and (b) and respective neighboring projections. Features are considered resolved as long as their correlation exceeds the half-bit criterion [22]. In the super-resolution (SR) reconstruction, the correlation is sustained beyond the Nyquist limit of the native image.

phase grating. The integration of this method into tomographic acquisition schemes was demonstrated using a photon-counting detector.

When compared to the full-field structured-illumination approach formulated by Günther et al. [12], our method achieves a comparable resolution gain while requiring only 25% of the acquisition steps needed for a two-dimensional reconstruction. As the maximal theoretically reconstructable frequency depends on the grating frequency, the same resolution gain can be achieved by reconstructing only the first order, provided the grating frequency is doubled. Thus, our proposed method would yield similar results with only nine translations. This approach may even surpass the resolution gain demonstrated for second-order harmonic reconstruction, as the first-order peak amplitude is higher (see Eq. 5). Similar to the approach by Günther et al. [12], the acquisition time does not scale with the size of the field of view (FOV), which differentiates our approach from classical STXM. Depending on the achieved resolution, STXM setups are typically limited to sample sizes on the order of $5\ \mu\text{m}$ [24] to a few $100\ \mu\text{m}$ [25]. This restriction arises from factors including the acquisition time, the limited depth of focus [24], and the travel range of the piezoelectric stages used for scanning [25]. In contrast, our method is well-suited for high-resolution, large FOV imaging in applications where resolution gain through magnifying optics is unsuitable. Large FOV imaging, such as demonstrated on rodent cochleas by Schaeper et al. [4], becomes feasible at higher resolutions due to our method. The reliance on

stitching multiple tomograms, as would typically be required when moving to a setup with larger geometric magnification, is thereby also alleviated. The resolution increase beyond the Nyquist limit is particularly relevant for photon-counting detectors, for which pixel sizes are presently limited to about $50\ \mu\text{m}$, since charge sharing becomes increasingly significant as pixel dimensions decrease [26]. Our approach enables surpassing this limit, as demonstrated in Sec. 2.3. In contrast to super-sampling methods such as proposed by Ehn et al. [27], our method does not rely on the performance of a deconvolution, but rather expands the pass-band independently of detection. Finally, our method is inherently multimodal. The method yields a super-resolved absorption image, while the same data support phase and dark-field reconstructions using unified modulated pattern analysis [28] (UMPA) or Fourier space methods [29, 30]. Unlike traditional Fourier space approaches, the component separation in our formulation enables higher resolution, as discussed by He et al. [31]. If the component separation is well optimized through phase-optimization algorithms [32–35], the resolution increase determined in He et al. [31] may even be exceeded. Further, for propagation-based phase contrast [36], our method may alleviate the resolution loss introduced by the low-pass filter.

These benefits notwithstanding, our method still requires multiple image acquisitions per projection. As the super-resolved projections have more pixels, the number of required acquisition angles in tomography increases accordingly. Both factors lead to longer acquisition times and substantially larger datasets. Efficiently reconstructing datasets of this size requires intensive computational effort. Moreover, the phase values derived from the stepping parameters may differ significantly from the optimal phase values gathered from optimization techniques [33], as discussed in Extended Data Fig. 4. This results in residual grating peaks, as explored in Extended Data Fig. 5. The resulting residual grating peaks reduce the achievable resolution gain and may introduce ring artifacts in tomographic reconstructions, as seen in Fig. 3 (d). Since the reconstruction involves multiple discrete Fourier transforms, additional artifacts arising from these computations may also occur.

These limitations highlight avenues for future development, which may enable broader applicability in X-ray imaging. Adopting high-frequency hexagonal grating structures would allow for an isometric frequency-space population with only seven steps for the first-order reconstruction. Moreover, because the super-resolution property is determined by the intensity distribution at the detector plane, an absorption grating positioned close to it can be used to produce structured illumination. This would alleviate the coherence required for this proof of principle. The necessary computational effort can be addressed by developing a GPU-accelerated reconstruction framework, which is justified as all processing steps are well parallelizable. In this context, more intensive iterative phase-optimization techniques [34] become practical to use within a tomographic framework, thereby improving reconstruction effectiveness and reducing artifacts.

3 Methods

3.1 Presence of Additional Image Information

Attenuation-based imaging contrast is commonly described by the Beer–Lambert law

$$I(x, y) = \int_0^{E_{\max}} I_0(E, x, y) \exp \left[- \int_0^d \mu(E, \eta, x, y) d\eta \right] dE, \quad (1)$$

where $I(x, y)$ is the intensity function after interaction with a sample, $I_0(E, x, y)$ is the incident spectral intensity distribution, and $\mu(E, \eta, x, y)$ denotes the linear attenuation coefficient as a function of photon energy E , depth within the sample η , and transverse position (x, y) . The variable d represents the total sample thickness. For the scope of the proposed proof-of-principle, it is sufficient to assume monochromaticity and abbreviate all sample-induced attenuation interaction into the function $S(x, y)$, yielding

$$I(x, y) = [I_0(x, y) \cdot S(x, y)] \otimes h(x, y). \quad (2)$$

where the additional convolution with the PSF $h(x, y)$ is induced by detection. Given that our method aims to increase resolution by exploiting the effects of periodic illumination on the spatial frequency content of an acquisition, it is natural to consider the Fourier-domain representation of this model. The Fourier transform of this product gives

$$\mathcal{F}\{I(x, y)\}(u, v) = [\mathcal{F}\{I_0(x, y)\}(u, v) \otimes \mathcal{F}\{S(x, y)\}(u, v)] \cdot O(u, v), \quad (3)$$

where \mathcal{F} denotes the Fourier transform operator, \otimes denotes the convolution arising from the convolution theorem, and $O(u, v) = \mathcal{F}\{h(x, y)\}(u, v)$ is the OTF. Since the illumination is presumed infinitely periodic, its spatial substructure may be described by five possible Bravais lattices. Following the rationale of Schropp et al. [37], only the square and hexagonal lattices are well suited for our purpose of Fourier-space analysis, as their basis vector magnitude is equal along both axes, thus populating the frequency space isotropically. Given that Gustschin et al. [38] have demonstrated the applicability of high-visibility two-dimensional square phase gratings, the illumination function $I_0(x, y)$ is henceforth assumed as an infinitely periodic square lattice:

$$I_0(x, y) = \bar{I} + a \left[\text{rect} \left((x - x_0) \frac{d}{wp}, (y - y_0) \frac{d}{wp} \right) - \frac{w}{d} \right] \otimes K(x, y) \otimes \text{III}_{p,p}, \quad (4)$$

where rect is the rectangular function and III is the Dirac comb. The arbitrary shift vector (x_0, y_0) originates from the possible asymmetry of the illumination pattern with respect to the coordinate origin. The convolution kernel K describes the blurring of the idealized illumination structure due to grating imperfections or partial coherence. The parameter p denotes the pattern period, and w/d is the opening ratio of the illumination. The factor a is the amplitude modulation, while \bar{I} is the mean intensity. Under

Fourier transformation, the convolution is expressed as a multiplication, resulting in

$$\begin{aligned}\mathcal{F}\{I_0(x, y)\}(u, v) &= I_a e^{-2\pi i(ux_0 + vy_0)} \left(p \frac{w}{d}\right)^2 \text{sinc}_\pi \left(p \frac{w}{d} u\right) \text{sinc}_\pi \left(p \frac{w}{d} v\right) \\ &\quad \cdot \mathcal{F}\{K(x, y)\}(u, v) \cdot \text{III}_{q,q} \\ &\equiv A(u, v) e^{i\varphi_0(u, v)} \cdot \text{III}_{q,q},\end{aligned}\tag{5}$$

where $\text{sinc}_\pi = \frac{\sin(\pi t)}{\pi t}$ denotes the normalised sinc function arising from the Fourier transform of the rectangular function. The reciprocal Dirac comb $\text{III}_{q,q}$ denotes the Fourier transform of the Dirac comb $\text{III}_{p,p}$. The frequency $q = \frac{1}{p}$ is the fundamental spatial frequency of the illumination pattern. The modulated intensity

$$I_a = \begin{cases} \bar{I} & u, v = 0, \\ a\bar{I} & \text{otherwise} \end{cases}\tag{6}$$

captures the case of pattern modulation a unequal to unity. The phase ramp $\exp(-2\pi i(ux_0 + vy_0)) \equiv \exp(i\varphi_0(u, v))$ originates from a possible asymmetry of the illumination pattern with respect to the origin. The prefactor $A(u, v)$ captures the amplitude behavior, including the effect of the blurring kernel $K(x, y)$ whose Fourier transform becomes a multiplicative factor. Substituting Eq. (5) into Eq. (3) yields

$$\begin{aligned}\mathcal{F}\{I(x, y)\}(u, v) &= \left[\left(A(u, v) e^{i\varphi_0(u, v)} \cdot \text{III}_{q,q} \right) \otimes \mathcal{F}\{S(x, y)\}(u, v) \right] \cdot O(u, v) \\ &= \sum_{n,m=-\infty}^{\infty} A_{(n,m)} e^{i\varphi_{0,(n,m)}} \mathcal{F}\{S(x, y)\}(u - nq, v - mq) \cdot O(u, v).\end{aligned}\tag{7}$$

So the Fourier transform of the intensity after the sample is a superposition of shifted sample-signal replicas, each centered at the respective (n,m) -th harmonic of the grating frequency. Each replic is multiplied with the corresponding prefactor $A_{(n,m)}$ and the constant phase factors $\exp(i\varphi_{0,(n,m)})$. Upon detection, the entire superposition is multiplied by the OTF $O(u, v)$. Notably, Eq. (7) in principle describes a superposition of infinitely many such replicas, provided that the coefficients $A_{(n,m)}$ remain non-zero.

3.2 Recovering additional information

Let $I_i(x, y)$ be the intensity distribution, shifted by (x_i, y_i) , after it traversed the sample. Using Eq. (7), the Fourier-domain representation can be written as

$$\begin{aligned}\mathcal{F}\{I_i(x, y)\}(u, v) &= [\mathcal{F}\{I_0(x - x_i, y - y_i)\} \otimes \mathcal{F}\{S(x, y)\}(u, v)] \cdot O(u, v) \\ &= \sum_{n,m=-\infty}^{\infty} e^{-2\pi i(ux_i + vy_i)} \Big|_{(u,v)=(nq,mq)} \\ &\quad \cdot A_{(n,m)} e^{i\varphi_{0,(n,m)}} \mathcal{F}\{S(x, y)\}(u - nq, v - mq) \cdot O(u, v)\end{aligned}\tag{8}$$

where the transverse pattern movement introduces a phase ramp in the corresponding dimension in Fourier space, which becomes discretized into a constant phase factor for each peak of the Dirac comb. Under convolution with the sample spectrum, each shifted replica of the sample spectrum inherits the corresponding constant phase factor. Due to the convolutional kernel $K(x, y)$, we assume that only a finite number of contributions to the sum have amplitudes higher than the noise level. For s_u peaks in dimension u and s_v peaks in dimensions v , a total number of $N = s_u s_v$ pattern translations with s_u steps in u and s_v in v are required to assign a distinct phase value to each peak. Thus, we can confine the harmonic indices to

$$m \in \left\{ -\frac{s_u - 1}{2}, \dots, \frac{s_u - 1}{2} \right\}, \quad n \in \left\{ -\frac{s_v - 1}{2}, \dots, \frac{s_v - 1}{2} \right\}, \quad (9)$$

which identify each harmonic displacement in the u - and v - directions, respectively. Similarly, the indices

$$\alpha \in \{0, \dots, s_u - 1\}, \quad \gamma \in \{0, \dots, s_v - 1\} \quad (10)$$

identify the associated pattern phase shift introduced during the raster scan. The phase factors associated with the harmonics (m, n) at the illumination steps (α, γ) are described by the 4D array

$$M_{\alpha m \gamma n} = \exp [i (\phi_{\alpha \gamma}^u m + \phi_{\alpha \gamma}^v n)]. \quad (11)$$

$\phi_{\alpha, \gamma}^{u, v}$ are elements of the set of all combinations of phases in (u, v) . Further, defining

$$i \equiv \gamma + \alpha \cdot s_v \quad \text{and} \quad j \equiv n' + m' \cdot s_u, \quad (12)$$

with $m' = m + (s_u - 1)/2$ and $n' = n + (s_v - 1)/2$, enables the construction of the matrix

$$M_{ij} = M_{\gamma + \alpha \cdot s_v, n' + m' \cdot s_u}. \quad (13)$$

of size $(s_u s_v) \times (s_u s_v)$. Thus, N image acquisitions in different pattern positions define a linear system [39] as

$$\tilde{I}_i(u, v) = M_{ij} \tilde{C}_j(u, v), \quad (14)$$

where $\tilde{I}_i = \mathcal{F}_{x, y} \{I_i\}$ and $\tilde{C}_j = \mathcal{F}_{x, y} \{C_j\}$, and $i \in \{0, \dots, N - 1\}$. The matrix $M_{ij} \in \mathbb{C}^{N \times N}$, with $j \in \{0, \dots, N - 1\}$ indexing the N components contributing to the superposition in Eq. (7), synthesizes the i -th image $\tilde{I}_i(x, y)$ from its corresponding set of basis components $\tilde{C}_j(x, y)$, each of which contains only the information contributed by a single shifted replica of the sample spectrum. So long as M_{ij} is invertible, Eq. (14) can be solved to reconstruct the basis components $\tilde{C}_j(u, v)$ of the form

$$\tilde{C}_j(u, v) = \tilde{C}_{(n, m)}(u, v) = A_{(n, m)} e^{i\varphi_{0, (n, m)}} \mathcal{F}\{S(x, y)\}(u - nq, v - mq) \cdot O(u, v). \quad (15)$$

Following the component expression in Eq. (15), the parameters q , $A_{(n, m)}$, and $\varphi_{0, (n, m)}$ must be accurately estimated to reliably extract the portion of the sample spectrum

embedded in the separated components. To determine the shift vector $\mathbf{q} = (nq, mq)^T$, we exploit that all components are frequency-shifted replicas of the sample spectrum. Consequently, wherever their information overlaps, this offers a reliable basis for the cross-correlation approach first described by Gustafsson et al. [40]. To compute this cross-correlation, the OTF associated with each separated component in Eq. (14) is removed by defining $\tilde{D}_{(n,m)}(u, v) \equiv \tilde{C}_{(n,m)}(u, v)O^*(u, v)/|O(u, v)|^2$, which is used only in this process of parameter estimation, but not in the final reconstruction. The shift vector is decomposed into an integer and a sub-integer component. The integer shift vector component is obtained straightforwardly using cross-correlation as

$$\mathbf{q}_{\text{int}} = \arg \max_{u, v \in \mathcal{F}, n, m \in \mathbb{Z}} (\tilde{D}_{(0,0)}(u, v) \star \tilde{D}_{(n,m)}(u, v)), \quad (16)$$

where \star denotes the correlation operator. After shifting each component by this vector, only a subpixel displacement remains. To accurately estimate this residual vector, we use the fact that a translation in Fourier space may be expressed as a phase ramp in real space. Thus, following the detailed presentation of Qian et al. [41], transforming each component into real space allows for a minimisation to yield the sub-pixel phase vector using the explicit cross-correlation over $\mathbf{r} = (x, y)^T$

$$\begin{aligned} CC_{(n,m)}(\mathbf{q}'_{\text{sub}}) &= \frac{\sum_{\mathbf{r}} A_{(n,m)} S_{(0,0)}^*(\mathbf{r}) S_{(n,m)}(\mathbf{r}) e^{i(\varphi_{0,(n,m)} + 2\pi\mathbf{r}(\mathbf{q}_{\text{sub}} - \mathbf{q}'_{\text{sub}}))}}{\sum_{\mathbf{r}} |S_{(0,0)}(\mathbf{r})|^2} \\ &= \frac{\sum_{\mathbf{r}} S_{(0,0)}^*(\mathbf{r}) D_{(n,m)}(\mathbf{r}) e^{i2\pi\mathbf{r}(\mathbf{q}_{\text{sub}} - \mathbf{q}'_{\text{sub}})}}{\sum_{\mathbf{r}} |S_{(0,0)}(\mathbf{r})|^2}. \end{aligned} \quad (17)$$

Here, $S_{(0,0)}^*$ is the complex conjugated zeroth-order real-space sample replica, $S_{(n,m)}$ is the real-space sample replica of order (n, m) , shifted by the integer component of \mathbf{q} . The vector \mathbf{q}'_{sub} represents a sub-pixel shift guess used in minimization. The value of \mathbf{q}'_{sub} for which $|CC_{(n,m)}|$ is maximal yields the desired sub-pixel shift \mathbf{q}_{sub} . Having estimated the sub-pixel shift vector, the parameters $A_{(n,m)}$ and $\varphi_{0,(n,m)}$ can be obtained by complex linear regression:

$$A_{(n,m)} = \left| \frac{\sum_{\mathbf{r}} A_{(n,m)} S_{(0,0)}^*(\mathbf{r}) S_{(n,m)}(\mathbf{r}) e^{i\varphi_0}}{\sum_{\mathbf{r}} |S_{(0,0)}(\mathbf{r})|^2} \right| = \left| \frac{\sum_{\mathbf{r}} S_{(0,0)}^*(\mathbf{r}) D_{(n,m)}(\mathbf{r})}{\sum_{\mathbf{r}} |S_{(0,0)}(\mathbf{r})|^2} \right| \quad (18)$$

$$\varphi_0 = \arg \left[\frac{\sum_{\mathbf{r}} A_{(n,m)} S_{(0,0)}^*(\mathbf{r}) S_{(n,m)}(\mathbf{r}) e^{i\varphi_0}}{\sum_{\mathbf{r}} |S_{(0,0)}(\mathbf{r})|^2} \right] = \arg \left[\frac{\sum_{\mathbf{r}} S_{(0,0)}^*(\mathbf{r}) D_{(n,m)}(\mathbf{r})}{\sum_{\mathbf{r}} |S_{(0,0)}(\mathbf{r})|^2} \right]. \quad (19)$$

Following this estimation, Gustafsson et al. [40] redefine the OTF such that these parameters are absorbed into it. Accordingly, defining

$$O'_{(n,m)}(u, v) = A_{(n,m)} e^{i\varphi_{0,(n,m)}} O(u, v) \quad (20)$$

enables the population of the super-resolved Fourier space through a generalized Wiener filter

$$\begin{aligned}\tilde{S}(u, v) &= \frac{\sum_{n,m} O'_{(n,m)}^*(u + nq, v + mq) \tilde{S}_{(n,m)}(u, v) O'_{(n,m)}(u + nq, v + mq)}{\sum_{n,m} |O'_{(n,m)}(u + nq, v + mq)|^2 + \epsilon^2} \\ &= \frac{\sum_{n,m} O'_{(n,m)}^*(u + nq, v + mq) \tilde{C}_{(n,m)}(u, v)}{\sum_{n,m} |O'_{(n,m)}(u + nq, v + mq)|^2 + \epsilon^2}\end{aligned}\quad (21)$$

where $\tilde{S}_{(n,m)}(u, v) = \mathcal{F}\{S(x, y)\}_{(n,m)}(u, v)$ are the separated sample replicas in Fourier space, shifted to their true position, as depicted in Fig. 1 (d-f, ii). The modulated OTFs are shifted according to the shift vector to retain their effects on their associated components. The parameter ϵ is a positive, empirically chosen regularization parameter. Since $\tilde{S}(u, v)$ is the Fourier representation of the super-resolved sample image, an inverse Fourier transformation of Eq. (21) yields the final real-space super-resolution reconstruction.

3.3 Experimental Setup for Test Pattern Acquisition

As discussed in Sec. 3.1, the reconstruction method requires a high-visibility illumination structure imposed on the sample projection. As had been established since Suleski et al. [42], a binary phase grating with a duty cycle of 1/3 and an induced phase shift of $2\pi/3$ produces a self-image at the fractional Talbot distance of $Z_T/6$, where Z_T denotes the Talbot distance. This has been experimentally demonstrated by Gustschin et al. [38] for highly coherent X-ray radiation and a 2D binary phase grating. For our experiment, a two-dimensional silicon phase grating with a period of $5\ \mu\text{m}$ was used as a wavefront marker at the P05 beamline [43, 44] at PETRA III at the Deutsches Elektronen-Synchrotron (DESY, Hamburg, Germany) at an X-ray energy of 18 keV. The grating is designed to induce a phase shift of $2\pi/3$ at 20 keV. A simulation found a fractional Talbot distance of 121 mm. Since the method also requires a translation of the structured illumination on the scale of the pattern period, the grating was mounted on a piezo-electric actuator. To determine the visibility of the Talbot illumination, the intensity variation recorded by each pixel during the stepping sequence is analysed to obtain a stepping profile for each pixel. The visibility change is then computed from this profile using Eq. 22. The resulting visibility map is shown in Extended Data Fig. 4 (d). The visibility value for the region discussed in Sec. 2.2 corresponds to the mean over this visibility map.

The scintillation screen is located at the position of highest theoretical visibility, when including effects from the convolutional kernel $K(x, y)$ in Eq. (4). The scintillator is coupled to an sCMOS pixelated detector [45] using a $5\times$ magnifying objective, resulting in an effective pixel size of $1.28\ \mu\text{m} \times 1.28\ \mu\text{m}$. To determine the PSF of the system, a circular aperture with a diameter of 1 mm was positioned as close to the detector as possible, and a series of 100 images was acquired. This was followed by the same number of dark-current and flat-field acquisitions. The exposure time was 60 ms for all measurements. The images were averaged to increase statistical reliability, and the PSF was reconstructed as detailed in Forster et al. [19].

The experiment was conducted using a resolution test pattern (model X500-200-30, Xradia, Pleasanton, USA; now ZEISS, Oberkochen, Germany) was positioned 2 mm upstream of the scintillator screen. For the depiction in Fig. 1, a set of 25 images was acquired in a 5×5 raster, with step sizes of $1 \mu\text{m}$ in both dimensions. This sampling strategy enables separation of the first- and second-harmonic orders under conditions of maximal variation in grating position across images. At each position, four exposures of 90 ms were averaged. This procedure was performed once with the sample in the beam path and once without to obtain a flat-field reference.

3.4 Experimental Setup for Tomographic Acquisition

The tomographic acquisition used for super-resolution reconstruction has previously been reported on by John et al. [21]. It was performed at the GINIX setup [46] of the beamline P10 at DESY using an Eiger X 4M photon-counting detector by DECTRIS AG (Baden-Daettwil, Switzerland) with a physical pixel size of $75 \mu\text{m} \times 75 \mu\text{m}$. As this beamline relies on a small source spot emerging from a waveguide [46], large geometric magnification is central to the imaging setup. Accordingly, the detector was positioned at a distance of 5090 mm from the waveguide. With the sample positioned at a distance of 260 mm from the waveguide, a magnification of 19.6 was achieved, yielding an effective pixel size of $3.84 \mu\text{m} \times 3.84 \mu\text{m}$ in the sample plane.

A two-dimensional binary phase grating, as described by Gustschin et al. [38], with a design period of $10 \mu\text{m}$ was positioned at a distance of 100 mm from the waveguide’s exit. It is designed to affect a $2\pi/3$ phase shift at an energy of 10 keV. The X-ray energy used in the experiment was 8 keV. Through a magnification of 50.9, its effective grating period in the detector plane was $509 \mu\text{m}$. In this setup, each grating period was sampled by 6.8 detector pixels, corresponding to a grating-to-detector frequency ratio of 3.4. To demonstrate that the methodology can be extended to tomography with a similar resolution increase and for higher harmonic orders, the relationship between the Nyquist and grating frequencies needs to be adjusted. Hence, the data set is downsampled, increasing the detector pixel size to $114 \mu\text{m} \times 114 \mu\text{m}$ and adjusting the ratio between the sampling and grating frequencies to 2.2. Consequently, both the first and second harmonic orders are firmly within the native Nyquist frequency. This does not restrict the generality of the demonstration, as a different magnification of the grating can achieve the appropriate frequency in the detector plane.

The tomography was acquired over a 360° angular range, with 250 equidistant angular projections. The exposure time was set to 1 s with an energy threshold of 4.4 keV. A total of 26 steps was acquired in the scheme detailed in Gustschin et al. [38] with $a = 1$ and $b = 5$, of which only 25 were used to reconstruct up to the second harmonic order. At each grating step, a full tomography was acquired.

3.5 Reconstruction

The super-resolution reconstruction for each projection is performed using a custom Python framework designed based on the descriptions in Sec. 3.1 and 3.2. The tomographic reconstruction is computed with the software X-AID (MITOS, Munich,

Germany).

For both the test pattern acquisition and the tomography, the reconstruction procedure was performed independently for the sample and reference datasets. The precise grating positions used to populate the matrix in Eq. (11) were estimated using the non-iterative approach described by Wicker et al. [33]. The final image for each projection was obtained by dividing the reconstructed sample image by the corresponding reference, yielding a properly scaled result. After the test pattern reconstruction, the extended pass-band is sampled with an effective pixel size of $0.64 \mu\text{m} \times 0.64 \mu\text{m}$. For analysis, the image was slightly rotated using a third-order spline interpolation to align the horizontal and vertical line patterns with their respective axes. Further, aliasing effects had to be compensated in the test pattern acquisition. If the PSF of an imaging system does not sufficiently suppress information outside the pass-band, aliasing artifacts may significantly influence the acquired image. In the case described in Sec. 2.1, the effective detector pixel pitch is $1.28 \mu\text{m}$. Given the grating design period of $5 \mu\text{m}$, the second-order harmonic is only marginally unresolved, resulting in an aliasing artifact in the Fourier domain of the acquisition. In the case presented here, this can be corrected by periodically shifting the Fourier image. This approach effectively suppresses dominant aliasing artifacts, provided two conditions are met. First, the frequency may only be unresolved by a marginal distance in frequency space, thereby minimizing the required pixel shift. Second, the peak must be well modulated, ensuring that its information amplitude is sufficiently dominant over the unaliased sample frequencies.

For the tomographic dataset, optimal synthetic references for each image were computed from a set of sample-free acquisitions, as described by Van Nieuwenhove et al. [47]. In the super-resolution reconstruction and parameter estimation procedure, the PSF is assumed to be box-shaped. After reconstruction, the extended pass-band is sampled by an effective pixel size of $2.04 \mu\text{m}$. The three-dimensional volume was reconstructed using filtered back-projection with a Ram-Lak filter in the software X-AID. Ring artefacts were removed using the proprietary filter implemented in the X-AID software.

3.6 Resolution Assessment

To determine the achievable resolution gain, a test pattern was imaged as detailed in Sec. 3.3. The resolution achieved for the test pattern (see Fig. 2) is quantified in terms of line-pair modulation defined by the visibility

$$M = \frac{I_{\max} - I_{\min}}{I_{\max} + I_{\min}}, \quad (22)$$

where I denotes the detected intensity. The maximal and minimal intensity values I_{\max} and I_{\min} were taken from the associated line-pair region after averaging along the axis perpendicular to the line-pattern. A line-pair is considered resolved when the modulation exceeds the 10% threshold [20].

The resolution gain achieved in the tomographic reconstruction was determined using

Fourier ring correlation [23]. For our purpose, a feature is considered resolved if its correlation exceeds the half-bit criterion [22].

Acknowledgements. We gratefully acknowledge the Helmholtz-Zentrum Hereon and the Deutsches Elektronen-Synchrotron for providing the required research infrastructure under the proposals BAG-20240009 and BAG-20240010. We also extend our gratitude to the beamline staff, namely Jörg Hammel and Felix Beckmann, for their continuous assistance. We further thank Prof. Julia Herzen for her assistance in organizing the beamtimes at DESY and Dominik John for fruitful discussions and for providing the tomography dataset. Benedikt Günther and Lennart Forster acknowledge funding by the Deutsche Forschungsgemeinschaft (513827659). We further acknowledge funding from the Centre for Advanced Laser Applications.

References

- [1] Thompson, A., Maskery, I., Leach, R.K.: X-ray computed tomography for additive manufacturing: a review. *Measurement Science and Technology* **27**(7), 072001 (2016) <https://doi.org/10.1088/0957-0233/27/7/072001>
- [2] Rathore, J.S., King, A., Le Bourdais, F., Garandet, J.-P.: In-depth analysis of CT resolution impact on porosity evaluation in laser powder bed fusion additive manufacturing. *Tomography of Materials and Structures* **8**, 100065 (2025) <https://doi.org/10.1016/j.tmater.2025.100065>
- [3] Villarraga-Gómez, H., Begun, D.L., Bhattad, P., Mo, K., Norouzi Rad, M., White, R.T., Kelly, S.T.: Assessing rechargeable batteries with 3D X-ray microscopy, computed tomography, and nanotomography. *Nondestructive Testing and Evaluation* **37**(5), 519–535 (2022) <https://doi.org/10.1080/10589759.2022.2070165>
- [4] Schaeper, J.J., Kampshoff, C.A., Wolf, B.J., Roos, L., Michanski, S., Ruhwedel, T., Eckermann, M., Meyer, A., Jeschke, M., Wichmann, C., Moser, T., Salditt, T.: 3D virtual histology of rodent and primate cochleae with multi-scale phase-contrast X-ray tomography. *Scientific Reports* **15**(1), 7933 (2025) <https://doi.org/10.1038/s41598-025-89431-0>
- [5] Busse, M., Müller, M., Kimm, M.A., Ferstl, S., Allner, S., Achterhold, K., Herzen, J., Pfeiffer, F.: Three-dimensional virtual histology enabled through cytoplasm-specific X-ray stain for microscopic and nanoscopic computed tomography. *Proceedings of the National Academy of Sciences* **115**(10), 2293–2298 (2018) <https://doi.org/10.1073/pnas.1720862115>
- [6] Preuss, A., Van De Kamp, T., Hamann, E., Zuber, M., Ornowski, L., Gorb, S.N.: Functional morphology of the leg musculature in the marine seal louse: adaptations for high-performance attachment to diving hosts. *Scientific Reports* **15**(1), 44732 (2025) <https://doi.org/10.1038/s41598-025-32804-2>

- [7] Sievert, R.M.: Two Methods of Roentgen Micro-Photography: Preliminary report. *Acta Radiologica Original Series Volume 17*(3), 299–309 (1936) <https://doi.org/10.1177/028418513601700308>
- [8] Cosslett, V.E., Nixon, W.C.: X-Ray Shadow Microscopy. *Nature* **170**(4324), 436–438 (1952) <https://doi.org/10.1038/170436a0>
- [9] Kirkpatrick, P., Baez, A.V.: Formation of Optical Images by X-Rays. *Journal of the Optical Society of America* **38**(9), 766 (1948) <https://doi.org/10.1364/JOSA.38.000766>
- [10] Snigirev, A., Kohn, V., Snigireva, I., Lengeler, B.: A compound refractive lens for focusing high-energy X-rays. *Nature* **384**(6604), 49–51 (1996) <https://doi.org/10.1038/384049a0>
- [11] Feggeler, T., Levitan, A., Marcus, M.A., Ohldag, H., Shapiro, D.A.: Scanning transmission X-ray microscopy at the Advanced Light Source. *Journal of Electron Spectroscopy and Related Phenomena* **267**, 147381 (2023) <https://doi.org/10.1016/j.elspec.2023.147381>
- [12] Günther, B., Hehn, L., Jud, C., Hipp, A., Dierolf, M., Pfeiffer, F.: Full-field structured-illumination super-resolution X-ray transmission microscopy. *Nature Communications* **10**(1), 2494 (2019) <https://doi.org/10.1038/s41467-019-10537-x>
- [13] Talbot, H.F.: LXXVI. *Facts relating to optical science. No. IV.* The London, Edinburgh, and Dublin Philosophical Magazine and Journal of Science **9**(56), 401–407 (1836) <https://doi.org/10.1080/14786443608649032>
- [14] Rayleigh, L.: XXV. *On copying diffraction-gratings, and on some phenomena connected therewith.* The London, Edinburgh, and Dublin Philosophical Magazine and Journal of Science **11**(67), 196–205 (1881) <https://doi.org/10.1080/14786448108626995>
- [15] Heintzmann, R., Cremer, C.G.: Laterally modulated excitation microscopy: improvement of resolution by using a diffraction grating. In: Bigio, I.J., Schneckenburger, H., Slavik, J., Svanberg, K., Viallet, P.M. (eds.) *Optical Biopsies and Microscopic Techniques III*, pp. 185–196. SPIE, Stockholm, Sweden (1999). <https://doi.org/10.1117/12.336833> . <http://proceedings.spiedigitallibrary.org/proceeding.aspx?articleid=972650>
- [16] Gustafsson, M.G.L.: Surpassing the lateral resolution limit by a factor of two using structured illumination microscopy: SHORT COMMUNICATION. *Journal of Microscopy* **198**(2), 82–87 (2000) <https://doi.org/10.1046/j.1365-2818.2000.00710.x>
- [17] Born, M., Wolf, E.: *Principles of Optics: Electromagnetic Theory of Propagation,*

Interference and Diffraction of Light, Seventh (expanded) edition, 13th printing edn. Cambridge University Press, Cambridge (2017)

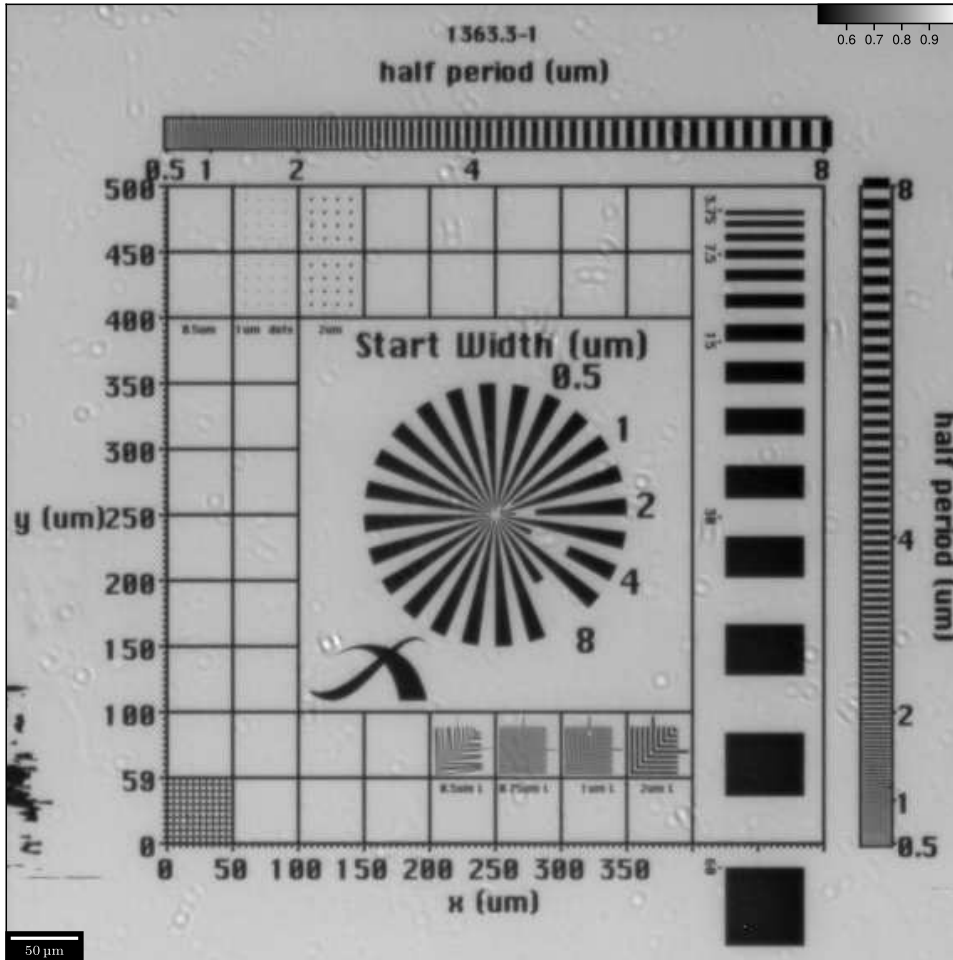
- [18] Wen, G., Li, S., Liang, Y., Wang, L., Zhang, J., Chen, X., Jin, X., Chen, C., Tang, Y., Li, H.: Spectrum-optimized direct image reconstruction of super-resolution structured illumination microscopy. *PhotonIX* **4**(1), 19 (2023) <https://doi.org/10.1186/s43074-023-00092-6>
- [19] Forster, L., Dierolf, M., Achterhold, K., Pfeiffer, F., Günther, B.: Single-shot 2D detector point-spread function analysis employing a circular aperture and a back-projection approach. *Optics Express* **33**(4), 7409 (2025) <https://doi.org/10.1364/OE.542925>
- [20] International Organization for Standardization: ISO 12233:2024 - Digital cameras - Resolution and spatial frequency responses. Standard, International Organization for Standardization, Geneva, CH (2024). <https://www.iso.org/standard/83705.html>
- [21] John, D., Breitenhuber, G., Wirtensohn, S., Hinterdobler, F., Gaetani, L., Savatovic, S., Lucht, J., Osterhoff, M., Eckermann, M., Salditt, T., Herzen, J.: Near-perfect efficiency in X-ray phase microtomography. *Optica* **13**(1) (2026) <https://doi.org/10.1364/OPTICA.584432>
- [22] Van Heel, M., Schatz, M.: Fourier shell correlation threshold criteria. *Journal of Structural Biology* **151**(3), 250–262 (2005) <https://doi.org/10.1016/j.jsb.2005.05.009> . Accessed 2024-04-18
- [23] Saxton, W.O., Baumeister, W.: The correlation averaging of a regularly arranged bacterial cell envelope protein. *Journal of Microscopy* **127**(2), 127–138 (1982) <https://doi.org/10.1111/j.1365-2818.1982.tb00405.x>
- [24] Aidukas, T., Phillips, N.W., Diaz, A., Poghosyan, E., Müller, E., Levi, A.F.J., Aeppli, G., Guizar-Sicairos, M., Holler, M.: High-performance 4-nm-resolution X-ray tomography using burst ptychography. *Nature* **632**(8023), 81–88 (2024) <https://doi.org/10.1038/s41586-024-07615-6>
- [25] Kilcoyne, A.L.D., Tyliczszak, T., Steele, W.F., Fakra, S., Hitchcock, P., Franck, K., Anderson, E., Harteneck, B., Rightor, E.G., Mitchell, G.E., Hitchcock, A.P., Yang, L., Warwick, T., Ade, H.: Interferometer-controlled scanning transmission X-ray microscopes at the Advanced Light Source. *Journal of Synchrotron Radiation* **10**(2), 125–136 (2003) <https://doi.org/10.1107/S0909049502017739>
- [26] Chmeissani, M., Mikulec, B.: Performance limits of a single photon counting pixel system. *Nuclear Instruments and Methods in Physics Research Section A: Accelerators, Spectrometers, Detectors and Associated Equipment* **460**(1), 81–90 (2001) [https://doi.org/10.1016/S0168-9002\(00\)01100-1](https://doi.org/10.1016/S0168-9002(00)01100-1)

- [27] Ehn, S., Epple, F.M., Fehringer, A., Pennicard, D., Graafsma, H., Noël, P., Pfeiffer, F.: X-ray deconvolution microscopy. *Biomedical Optics Express* **7**(4), 1227 (2016) <https://doi.org/10.1364/BOE.7.001227>
- [28] Zdora, M.-C., Thibault, P., Zhou, T., Koch, F.J., Romell, J., Sala, S., Last, A., Rau, C., Zanette, I.: X-ray Phase-Contrast Imaging and Metrology through Unified Modulated Pattern Analysis. *Physical Review Letters* **118**(20), 203903 (2017) <https://doi.org/10.1103/PhysRevLett.118.203903>
- [29] Bennett, E.E., Kopace, R., Stein, A.F., Wen, H.: A grating-based single-shot x-ray phase contrast and diffraction method for *in vivo* imaging. *Medical Physics* **37**(11), 6047–6054 (2010) <https://doi.org/10.1118/1.3501311>
- [30] Wen, H., Bennett, E.E., Hegedus, M.M., Carroll, S.C.: Spatial Harmonic Imaging of X-ray Scattering—Initial Results. *IEEE Transactions on Medical Imaging* **27**(8), 997–1002 (2008) <https://doi.org/10.1109/TMI.2007.912393>
- [31] He, C., Sun, W., MacDonald, C.A., Petrucci, J.C.: The application of harmonic techniques to enhance resolution in mesh-based x-ray phase imaging. *Journal of Applied Physics* **125**(23), 233101 (2019) <https://doi.org/10.1063/1.5094167>
- [32] Shroff, S.A., Fienup, J.R., Williams, D.R.: Phase-shift estimation in sinusoidally illuminated images for lateral superresolution. *Journal of the Optical Society of America A* **26**(2), 413 (2009) <https://doi.org/10.1364/JOSAA.26.000413>
- [33] Wicker, K.: Non-iterative determination of pattern phase in structured illumination microscopy using auto-correlations in Fourier space. *Optics Express* **21**(21), 24692 (2013) <https://doi.org/10.1364/OE.21.024692>
- [34] Wicker, K., Mandula, O., Best, G., Fiolka, R., Heintzmann, R.: Phase optimisation for structured illumination microscopy. *Optics Express* **21**(2), 2032 (2013) <https://doi.org/10.1364/OE.21.002032>
- [35] Cao, R., Chen, Y., Liu, W., Zhu, D., Kuang, C., Xu, Y., Liu, X.: Inverse matrix based phase estimation algorithm for structured illumination microscopy. *Biomedical Optics Express* **9**(10), 5037 (2018) <https://doi.org/10.1364/BOE.9.005037>
- [36] Paganin, D., Mayo, S.C., Gureyev, T.E., Miller, P.R., Wilkins, S.W.: Simultaneous phase and amplitude extraction from a single defocused image of a homogeneous object. *Journal of Microscopy* **206**(1), 33–40 (2002) <https://doi.org/10.1046/j.1365-2818.2002.01010.x>
- [37] Schropp, M., Uhl, R.: Two-dimensional structured illumination microscopy. *Journal of Microscopy* **256**(1), 23–36 (2014) <https://doi.org/10.1111/jmi.12154>
- [38] Gustschin, A., Riedel, M., Taphorn, K., Petrich, C., Gottwald, W., Noichl, W.,

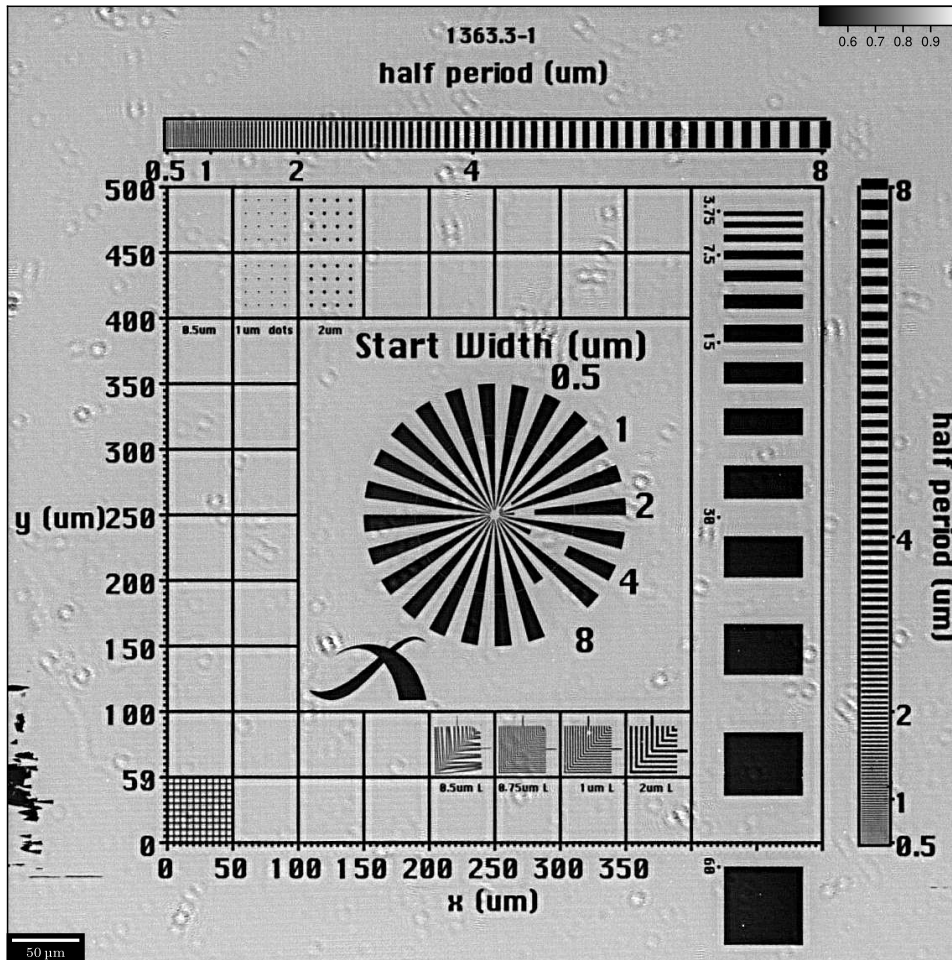
- Busse, M., Francis, S.E., Beckmann, F., Hammel, J.U., Moosmann, J., Thibault, P., Herzen, J.: High-resolution and sensitivity bi-directional x-ray phase contrast imaging using 2D Talbot array illuminators. *Optica* **8**(12), 1588 (2021) <https://doi.org/10.1364/OPTICA.441004>
- [39] Heintzmann, R.: Saturated patterned excitation microscopy with two-dimensional excitation patterns. *Micron* **34**(6-7), 283–291 (2003) [https://doi.org/10.1016/S0968-4328\(03\)00053-2](https://doi.org/10.1016/S0968-4328(03)00053-2)
- [40] Gustafsson, M.G.L., Shao, L., Carlton, P.M., Wang, C.J.R., Golubovskaya, I.N., Cande, W.Z., Agard, D.A., Sedat, J.W.: Three-Dimensional Resolution Doubling in Wide-Field Fluorescence Microscopy by Structured Illumination. *Biophysical Journal* **94**(12), 4957–4970 (2008) <https://doi.org/10.1529/biophysj.107.120345>
- [41] Qian, J., Cao, Y., Bi, Y., Wu, H., Liu, Y., Chen, Q., Zuo, C.: Structured illumination microscopy based on principal component analysis. *eLight* **3**(1), 4 (2023) <https://doi.org/10.1186/s43593-022-00035-x>
- [42] Suleski, T.J.: Generation of Lohmann images from binary-phase Talbot array illuminators. *Applied Optics* **36**(20), 4686 (1997) <https://doi.org/10.1364/AO.36.004686>
- [43] Greving, I., Wilde, F., Ogurreck, M., Herzen, J., Hammel, J.U., Hipp, A., Friedrich, F., Lottermoser, L., Dose, T., Burmester, H., Müller, M., Beckmann, F.: P05 imaging beamline at PETRA III: first results. In: Stock, S.R. (ed.) *Developments in X-Ray Tomography IX*, p. 92120. SPIE, San Diego, California, United States (2014). <https://doi.org/10.1117/12.2061768> . <http://proceedings.spiedigitallibrary.org/proceeding.aspx?doi=10.1117/12.2061768>
- [44] Wilde, F., Ogurreck, M., Greving, I., Hammel, J.U., Beckmann, F., Hipp, A., Lottermoser, L., Khokhriakov, I., Lytaev, P., Dose, T., Burmester, H., Müller, M., Schreyer, A.: Micro-CT at the imaging beamline P05 at PETRA III. In: *AIP Conference Proceedings*, p. 030035. AIP, New York, NY USA (2016). <https://doi.org/10.1063/1.4952858> . <https://pubs.aip.org/aip/acp/article/821251>
- [45] Lytaev, P., Hipp, A., Lottermoser, L., Herzen, J., Greving, I., Khokhriakov, I., Meyer-Loges, S., Plewka, J., Burmester, J., Caselle, M., Vogelgesang, M., Chilingaryan, S., Kopmann, A., Balzer, M., Schreyer, A., Beckmann, F.: Characterization of the CCD and CMOS cameras for grating-based phase-contrast tomography. In: Stock, S.R. (ed.) *Developments in X-Ray Tomography IX*, p. 921218. SPIE, San Diego, California, United States (2014). <https://doi.org/10.1117/12.2061389> . <http://proceedings.spiedigitallibrary.org/proceeding.aspx?doi=10.1117/12.2061389>
- [46] Kalbfleisch, S., Neubauer, H., Krüger, S.P., Bartels, M., Osterhoff, M., Mai, D.D., Giewekemeyer, K., Hartmann, B., Sprung, M., Salditt, T., McNulty, I., Eyberger, C., Lai, B.: The Göttingen Holography Endstation of Beamline P10 at

PETRA III DESY. In: AIP Conference Proceedings, pp. 96–99. AIP, Chicago, Illinois, (USA) (2011). <https://doi.org/10.1063/1.3625313> . <https://pubs.aip.org/aip/acp/article/1365/1/96-99/872026>

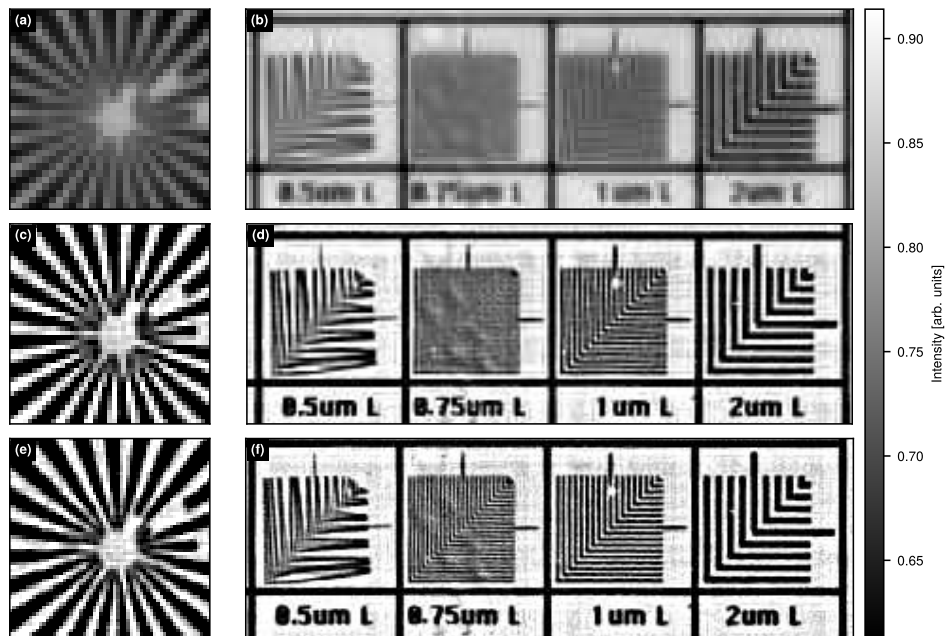
- [47] Van Nieuwenhove, V., De Beenhouwer, J., De Carlo, F., Mancini, L., Marone, F., Sijbers, J.: Dynamic intensity normalization using eigen flat fields in X-ray imaging. *Optics Express* **23**(21), 27975 (2015) <https://doi.org/10.1364/OE.23.027975>



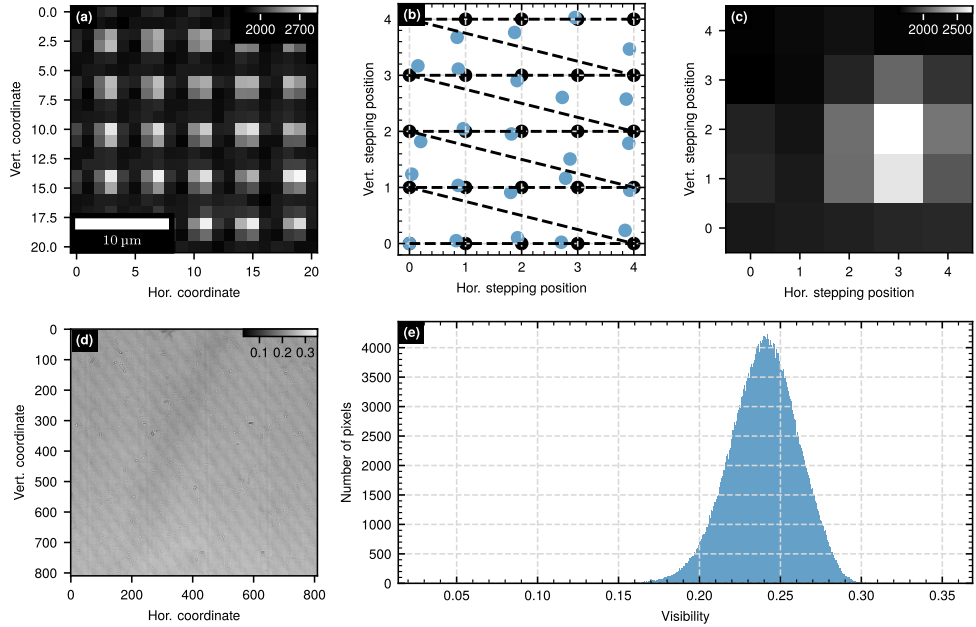
Extended Data Fig. 1 Native projection image of the resolution test pattern. The colorbar indicates the normalized intensity.



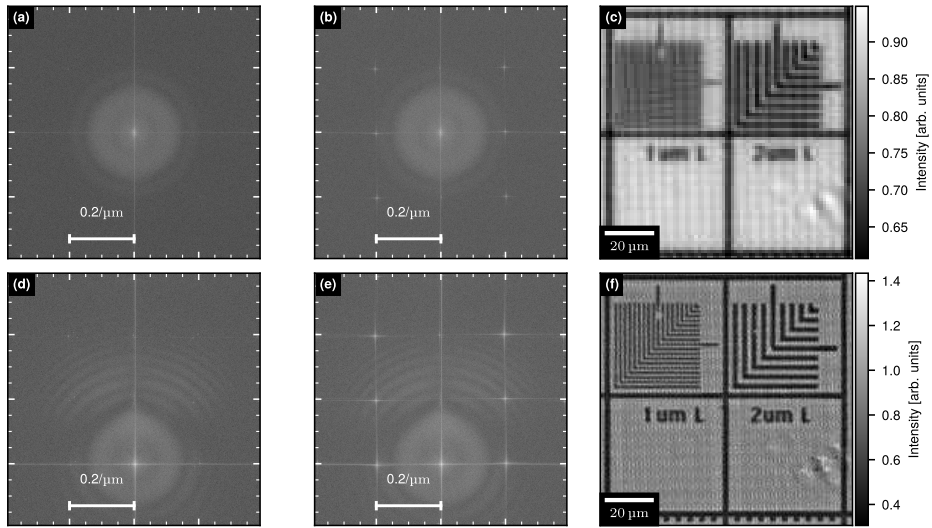
Extended Data Fig. 2 Super-resolved projection image of the resolution test pattern. The colorbar indicates the normalized intensity.



Extended Data Fig. 3 Qualitative comparison of resolution gain between first- and second-order reconstruction. (a) Native image of the center region of the Siemens star in the middle of the test pattern marked in green in Fig. 2 (a). (b) Native image of the L-shaped resolution target, marked in orange in Fig. 2 (a). (c) and (d) show the first-order super-resolved image of the regions in (a) and (b), respectively. (e) and (f) are the second-order super-resolved images of (a) and (b), respectively, shown also in Fig. 2 (e) and (f). While a qualitative assessment shows an improvement in resolution in the first-order reconstruction, as evidenced by the modulation in the $1\ \mu\text{m}$ resolution target, the modulation is higher in the second-order reconstruction. (a-b) and (e-f) were already shown in Fig. 2, but are presented here again to demonstrate the transition in resolution gain.



Extended Data Fig. 4 Visibility analysis of the utilized grating. (a) Shows an exemplary region of the illumination pattern created by the grating. (b) displays the nominal grating positions relative to those determined by the phase optimization. (c) presents the resulting stepping profile of an arbitrary exemplary pixel. This profile is determined by recording the detected intensity at each pixel as a function of grating position. The colorbars in (a) and (c) indicate the raw detector counts. (d) is the visibility map over the full region in which the test pattern reconstruction was computed. It is determined from the stepping profile in each pixel using Eq. 22. (e) shows the number of pixels per visibility determined from their stepping profile.



Extended Data Fig. 5 Effects of inaccurate phase estimation in the separation matrix.

(a) shows the logarithmic absolute value of the separated zero-order component of the reference scan after optimizing the phase values following the approach of Wicker et al. [33]. (b) shows the same projection component, separated under the assumption of equidistant stepping. (c) presents the native projection image computed as the absolute value of the inverse Fourier transform of (b). Inaccurate phase estimation in the separation matrix leads to a residual grating structure. (d) and (e) display the logarithmic absolute value of the first-order components of the reference scan again with (d) and without (e) phase optimization. (f) displays the second-order super-resolved reconstruction under the assumption of equidistant stepping. This inaccurate assumption leads to the visible grating remnants and less resolution gain than demonstrated in Sec. 2.2.